MOCVD of Bismuth Oxides: Transport Properties and Deposition Mechanisms of the $Bi(C_6H_5)_3$ Precursor

C. Bedoya, G. G. Condorelli, G. Anastasi, A. Baeri, F. Scerra, and I. L. Fragalà*

Dipartimento di Scienze Chimiche, Università di Catania, Catania, Italy

J. G. Lisoni and D. Wouters

IMEC, Leuven, Belgium

Received January 30, 2004. Revised Manuscript Received June 1, 2004

Deposition processes of bismuth oxides have been investigated using the $Bi(C_6H_5)_3$ precursor. The role of the MOCVD parameters has been evaluated through the study of both the precursor sublimation and the entire CVD process depending on the temperature and the reactor environment. In the 350−450 °C range, Bi_2O_3 deposition follows a heterogeneous pathway leading to the dissociation of Bi−phenyl bonds. O_2 plays a determining role in both the precursor decomposition and Bi_2O_3 growth. Above 450 °C, the oxidative break-down of the aromatic ring has been also observed. The temperature effect on Bi_2O_3 growth on platinum and iridium substrates has been investigated by grazing incident X-ray diffraction, SEM, and EDX measurements. Overall results indicate that a heterogeneous process predominantly controls the Bi_2O_3 deposition.

Introduction

The fabrication of Bi-containing materials is of growing interest due to their applications in several technological fields. Bi_2O_3 exhibits remarkably useful solid-state properties. The high-temperature form δ-Bi_2O_3 is among the best ionic conductors, while deliberately doped specimens of β-Bi_2O_3 exhibit a promising ionic conductivity.[1,2] Many multicomponent catalysts, such as ternary oxides of Bi and Mo, are widely used in a variety of heterogeneous oxidations and ammoxidations of alkenes and hydrocarbons.[3]

Bismuth oxide thin films are also of great interest due to the significant band gap (2.85 and 2.58 eV for the monoclinic α-Bi_2O_3 and tetragonal β-Bi_2O_3 phases, respectively),[4−6] high refractive index and dielectric permittivity, as well as marked photoconductivity and photoluminescence.[7,8] These properties make Bi_2O_3 films well suited for many applications in various domains such as microelectronics,[9] sensor technology,[10] optical coatings,[11] and ceramic glass manufacturing.[12] Bi_2O_3-based layered-perovskites belonging to the Aurivillius family are promising materials for superconducting electronics and nonvolatile ferroelectric memories (NVFeRAM).[13−21] Among ferroelectric oxides, $SrBi_2Ta_2O_9$ (SBT) has a superior endurance resistance compared to other ferroelectric perovskites such as $(Pb_xZr_{1-x})TiO_3$.[13,14] Recently, $(Bi_{1-x}La_x)_4Ti_3O_{12}$ (BLT) has been introduced, promising a better remnant polarization, lower processing temperature, and similar endurance reliability.[17−20] The main reason preventing the widespread commercialization of NVFeRAMs so far has been the lack of successful integration of the deposition processes of these materials with established Si-based CMOS technologies. High-level integration required by commercially competitive 1T1C stacked ferroelectric cells is entirely suited to MOCVD due to the better conformality of deposition over these 3-dimensional cell structures and a higher throughput compared to that of other

* To whom correspondence should be addressed. E-mail: lfragala@dipchi.unict.it.

(1) Zhou, W.; Jefferson, D. A.; Alario-Franco, M.; Thomas, J. M. *J. Phys. Chem.* **1987**, *91*, 512.
(2) Kharton, V. V.; Naumovich, E. N.; Yaremchenko, A. A.; Marques, F. M. B. *J. Solid State Electron.* **2001**, *5*, 160.
(3) Barreca, D.; Morazzoni, F.; Rizzi, G. A.; Scotti, R.; Tondello, E. *Phys. Chem. Chem. Phys.* **2001**, *3*, 1743.
(4) Gobrecht, H.; Seeck, S.; Bergt, H. E.; Martens, A.; Kossmann, K. *Phys. Stat. Sol.* **1969**, *33*, 599.
(5) Gobrecht, H.; Seeck, S.; Bergt, H. E.; Martens, A.; Kossmann, K. *Phys. Status Solidi* **1969**, *34*, 569.
(6) Dolocan, V. *Appl. Phys.* **1978**, *16*, 405.
(7) Leontie, L.; Caraman, M.; Alexe, M.; Harnagea, C. *Surf. Sci.* **2002**, *507*−*510*, 480.
(8) Leontie, L.; Caraman, M.; Delibas, M.; Rusu, G. I. *Mater. Res. Bull* **2001**, *36*, 1629.
(9) Bandoli, G.; Barecca, D.; Brescacin, E.; Rizzi, G. A.; Tondello, E. *Chem. Vap. Deposition* **1996**, *2*, 238.
(10) Hyodo, T.; Kanazawa, E.; Takao, Y.; Shimizu, Y.; Egashira, M. *Electrochemistry* **2000**, *68*, 24.
(11) Schuisky, M.; Härsta, A. *Chem. Vap. Deposition* **1996**, *2*, 235.
(12) Pan, A.; Ghosh, A. *J. Non-Cryst. Solids* **2000**, *271*, 2157.
(13) Araujo, C. A.; Cuchiaro, J. D.; McMillan, L. D.; Scott, M. C.; Scott, J. F. *Nature* **1989**, *374*, 627.
(14) Parker, L. H.; Tasch, A. F. *IEEE Circuit Devices Magn.* **1990**, *6*, 17.
(15) Aurivillius, B. *Ark. Kemi* **1949**, *1*, 463.
(16) Cummins, S. E.; Cross, L. E. *Appl. Phys. Lett.* **1967**, *10*, 14.
(17) Kingon, A. *Nature* **1999**, *401*, 658.
(18) Chu, M. W.; Ganne, M.; Tessier, P. Y.; Eon, D.; Caldes, M. T.; Brohan, L. *Mater. Sci. Semicond. Process.* **2002**, *5*, 179.
(19) Hardy, A.; Van Werde, K.; Vanhoyland, G.; Van Bael, M. K.; Mullens, J.; Van Poucke, L. C. *Thermochim. Acta* **2003**, *397*, 143.
(20) Bu, S. D.; Kang, B. S.; Park, B. H.; Noh, T. W. *J. Korean Phys. Soc.* **2000**, *36*, 9.
(21) Williams, P. A.; Jones, A. C.; Crosbie, M. J.; Wright, P. J.; Bickley, J. F.; Steiner, A.; Davis, H. O.; Leedham, T. L.; Critchlow, G. W. *Chem. Vap. Deposition* **2001**, *7*, 205.

10.1021/cm049836h CCC: $27.50 © 2004 American Chemical Society
Published on Web 07/15/2004

Table 1. Typical Bi Precursors for MOCVD Applications

family	precursor	application	ref.
Aryl	$Bi(C_6H_5)_3$	ferroelectrics (SBT, BLT, SBN), optic films, superconductors (BSCCO), gas sensors	3, 7, 17−20, 24−36
	$Bi(o\text{-}C_7H_7)_3$	ferroelectrics	37
β-diketonate	$Bi(C_{11}H_{19}O_2)_3$	ferroelectrics	38
Alkyls	$Bi(CH_3)_3$	ferroelectrics	25, 39−43
Alkoxyde	$Bi(OC(CH_3)_2CH_2OCH_3)_3$	ferroelectrics, superconductors	21, 24, 44−45

commercially available deposition techniques such as chemical solution deposition (CSD) and PVD.[22,23]

Recently, different Bi precursors have been proposed for MOCVD applications (Table 1).

Bismuth tri-phenyl ($Bi(C_6H_5)_3$) represents to date the most used precursor for the various MOCVD applications (Table 1). It shows remarkable advantages compared to other precursors in terms of thermal stability and clean sublimation. β-diketonates suffer from severe drawbacks due to their easy degradation under storage and upon sublimation. Therefore, they usually require reactors equipped with direct liquid injector systems (DLI) to obtain efficient MOCVD processes. On the other hand, $Bi(CH_3)_3$ possesses a good volatility, but is highly reactive and potentially explosive so it is poorly suited for practical use.[42] Recently $Bi(OC(CH_3)_2CH_2OCH_3)_3$ was shown to be suitable for deposition with Sr−Ta alkosides, but it exhibits thermal stability lower than $Bi(C_6H_5)_3$ and it requires DLI systems for applicable MOCVD processes. [24,44]

By contrast, $Bi(C_6H_5)_3$ is more versatile and can be efficiently used in both classical and DLI-equipped MOCVD reactors. Moreover, $Bi(C_6H_5)_3$ has proved to be a more suitable source than classic β-diketonates for DLI-MOCVD of BLT films in systems adopting a single solution source for three precursors[26] since it is less involved in unwanted side-reactions. In this wide context, very little information is available on the mechanistic aspects of MOCVD using a $Bi(C_6H_5)_3$ precursor. Recently, some data on the combined deposition kinetics of $Bi(C_6H_5)_3$ in the presence of $Ta(OC_2H_5)_5$ and $Sr(hfac)_2$-tetraglyme[46] have been presented. Similarly, the morphologies of films obtained by $Bi(C_6H_5)_3$−$Ta(OiPr)_4$(tmhd)− $Sr(tmhd)_2$tetraglyme precursor combination[29] have been reported. Nevertheless, many aspects of the $Bi(C_6H_5)_3$ decomposition mechanism during typical MOCVD processes are still unknown. The aim of the present paper is the study of the heterogeneous and homogeneous decomposition pathways of $Bi(C_6H_5)_3$ occurring in the MOCVD of bismuth oxides. FT-IR in situ monitoring was used to evaluate precursor thermal stability in mass transport. Insights on the deposition mechanism were obtained by combining FT-IR in situ monitoring of the gas phase with the study of the deposition kinetics.

A deep knowledge of precursor decomposition processes is relevant for the optimization of MOCVD processes and can be a useful starting point for selecting suitable precursor combinations for multicomponent processes.

Experimental Section

Bismuth tri-phenyl was purchased from Merck (99+%). It is a moisture-stable white powder (mp 78 °C). The vapor pressure, estimated with a bubbler apparatus, is around 13 Pa at 80 °C.[27] Thermogravimetric analyses were performed using a Mettler Toledo TGA/SDTA 851^e under purified N_2 flow (60 sccm). Temperatures ranged from 25 to 450 °C with a heating rate of 5 °C/min.

In situ FTIR measurements were performed in a MOCVD hot-wall reactor interfaced with a 4600/FT/IR 430 Jasco spectrometer. The MOCVD hot-wall quartz reactor has a total length of 15 cm with both a perpendicular gas inlet and gas outlet (relative to the reactor longitudinal axis) and a glass evaporator. A detailed description of the experimental apparatus has been reported elsewhere.[47] The precursor sublimation and MOCVD process were studied in the 130−280 °C and 200−550 °C ranges, respectively.

Depositions were performed in a reduced-pressure, horizontal, cold-wall MOCVD reactor consisting of contiguous sections (independently heated within ±2 °C using computer-controlled hardware) for precursor sublimation, gas mixing, and film deposition (total length 80 cm, i.d. 8 cm).

Films were deposited on $Pt/TiN/SiO_2/Si$ and $Ir/TiN/SiO_2/Si$ substrates. Pt and Ir substrates are of interest since they are suitable bottom electrodes in ferroelectric capacitors.[22,23] These multilayer substrates were prepared as follows: TiN, Ir, and

(22) Ramesh, R.; Aggarwal, S.; Auciello, O. *Mater. Sci. Eng., R* **2001**, *32*, 191.
(23) Zambrano, R. *Mater. Sci. Semicond. Process.* **2002**, *5*, 305.
(24) Jones, A. C.; Chalker, P. R. *J. Phys. D: Appl. Phys.* **2003**, *36*, 80.
(25) Isobe, C.; Hironaka, K.; Hishikawa, S. *Adv. Mater. Opt. Electron.* **2000**, *10*, 183.
(26) Kang, S. W.; Rhee S.-W. *J. Electrochem. Soc.* **2003**, *150*, C573.
(27) Isobe, C.; Sigiyama, M.; Hironaka, K.; Ami, T. U.S. Patent 6,-004,392, 1999.
(28) Jimbo, T.; Sano, H.; Takahashi, Y.; Funakubo, I.; Tokumizu, E.; Ishiwara, H. *Jpn. J. Appl. Phys.* **1999**, *38*, 6456.
(29) Roeder, J. F.; Hendrix, B. C.; Hintermaier, F.; Desrochers, D. A.; Baum, T. H.; Bhandari, G.; Chappuis, M.; Van Buskirk, P. C.; Dehm, C.; Fritsch, E.; Nagel, N.; Wendt, H.; Cerva, H.; Honlein, W.; Mature, C. *J. Eur. Ceram. Soc.* **1999**, *19*, 1463.
(30) Shin, W. C.; Choi, K. J.; Yoon, S. G. *Thin Solid Films* **2002**, *409*, 133.
(31) Zhu, Y.; Desu, S. B.; Li, T.; Ramanathan, S.; Nagata, M. *J. Mater. Res.* **1997**, *12*, 783.
(32) Li, T.; Zhu, Y.; Desu, S. B.; Peng, C. H.; Nagata, M. *Appl. Phys. Lett.* **1996**, *68*, 616.
(33) Sun, S.; Lu. P.; Fuierer A. *J. Cryst. Growth* **1999**, *205*, 177.
(34) Shimanoe K.; Suetsugu, M.; Miura, N.; Yamazoe, N. *Solid State Ionics* **1998**, *113*−*115*, 415.
(35) Neuman, G. A.; Bloss, K. H. U.S. Patent 4,965,093, 1990; p 4.
(36) Berry, A. D.; Holm, R. T.; Fatemi, M.; Giaskill, D. K. *J. Mater. Res.* **1990**, *5*, 1169.
(37) Kijima, T.; Ushikubo, M.; Matsunaga, H. *Jpn. J. Appl. Phys.* **1999**, *38*, 127.
(38) Van Buskirk, P. C.; Bilodeau, S. M.; Roeder, J. F.; Kirlin, P. S. *Jpn. J. Appl. Phys.* **1996**, *35*, 2520.
(39) Sakai, T.; Watanabe, T.; Choi, Y.; Matsuarai, K.; Funakubo, H. *Jpn. J. Appl. Phys.* **2001**, *40*, 6481.
(40) Funakubo, H.; Ishikawa, K.; Watanabe, T.; Mitsuya, M.; Nukaga, N. *Adv. Mater. Opt. Electron.* **2000**, *10*, 193.
(41) Nukaga, N.; Ono, H.; Shida, T.; Machida, H.; Suzuki, T.; Funakubo, H. *Integr. Ferroelectr.* **2002**, *4*, 215.
(42) Ishikawa, K.; Funakubo, H. *Appl. Phys. Lett.* **1999**, *75*, 1970.
(43) Funakubo, H.; Nukaga, N.; Ishikawa, K.; Watanabe, T. *Jpn. J. Appl. Phys.* **1999**, *38*, L199.
(44) Jones, A. *J. Mater. Chem.* **2002**, *12*, 2576.
(45) Herrmann, W. A.; Huber, N. W.; Anwaner, R.; Priermeier, T. *Chem. Ber.* **1993**, *126*, 1127.
(46) Condorelli, G. G.; Baeri, A.; Anastasi, G.; Fragalà, I. L. *Mater. Sci. Semicond. Proc.* **2003**, 5, 16.
(47) Condorelli, G. G.; Gennaro, S.; Fragalà, I. L. *Chem. Vap. Deposition* **2000**, *6*, 185.

Table 2. Assignments of Relevant IR Bands of $Bi(C_6H_5)_3$

wavenumber (cm^{-1})[a]	assignments of vibrations
3060 vs	aromatic hydrogen stretching
1955 w, 1885 w, 1805 w	overtone and combination bands
1570 m, 1476 m, 1430 m	benzene ring stretching
1187 w, 1055 m, 1014 m, 997 m	in-plane hydrogen bending
725 vs, 695 s	out-of-plane hydrogen bending

[a] s = strong; v = very; m = medium; w = weak.

Pt layers were deposited by a conventional sputtering technique on P-type Si(100) wafers with 250-nm phosphor-doped SiO_2 oxide. TiN was used as an adhesion layer for the Ir and Pt films. The multilayer substrates were placed on the susceptor (Advanced Ceramics Boralectric heating element) heated between 300 and 550 °C and at a total pressure in the 6−10 Torr range. Typical MOCVD conditions adopted prepurified Ar (99.999%) as carrier gas (100 sccm) and O_2 (O_2 99.999%) as reaction gas (500 sccm).

Precursor partial pressure (P_{Bi}) was varied by tuning the sublimation temperature in the 130−160 °C range. In all experiments P_{Bi} was calculated from the total quantity of the sublimed precursor determined by weight loss measurements according to the transpiration process reported by Temple and Reisman.[48]

Grazing incident X-ray diffraction (GIXRD) was performed with a Bruker AXS D5005 X-ray diffractometer equipped with a copper anode operated at 40 kV and 30 mA, Soller slits, Göebel mirror, and an attachment for thin film measurements. Measurements were performed with a detector scan from 20° < 2θ < 60°. The angle between the X-ray source and the sample surface was fixed at 0.5°.

Surface morphologies and film compositions were analyzed by scanning electron microscopy (SEM), performed with a LEO 1400 series. The microscope was equipped with energy dispersive X-ray (EDX) microanalysis.

Film thicknesses were estimated from the intensity ratio of the Bi M_α line (I_{Bi}) and the Pt or Ir M_α line (I_{Sub}) obtained by EDX measurements. The calibration curve between the I_{Bi}/I_{Sub} ratio and film thickness was determined on standard samples whose thicknesses were obtained by SEM cross section.

X-ray photoelectron spectroscopy (XPS) measurements were performed with a PHI 5600 Multy Technique System equipped with an Al standard X-ray source operating at 14 kV and a hemispherical analyzer. The electron takeoff angle (θ) was 45°. Sputter etching was performed with a 4 kV Ar^+ gun rastered over a 3 × 3 mm area. Depth profiles were obtained by alternating sputter etching and XPS analysis.

Results and Discussion

Preliminary Experiments. Preliminary gas- and solid-phase FTIR spectra of $Bi(C_6H_5)_3$ were recorded to provide a suitable database to monitor the MOCVD processes. Main frequencies and assignments are listed in Table 2.[26,49,50]

Some FT-IR experiments were performed to determine a calibration plot between the absorbances of characteristic bands of gas-phase $Bi(C_6H_5)_3$ (3060 and 725 cm^{-1}) and P_{Bi}. These experiments showed that absorbance of bands at 3060 and 725 cm^{-1} is directly proportional to P_{Bi} and can be used to monitor gas-phase composition.

Sublimation Process. The sublimation process was studied in the 25−450 °C range by TG measurements.

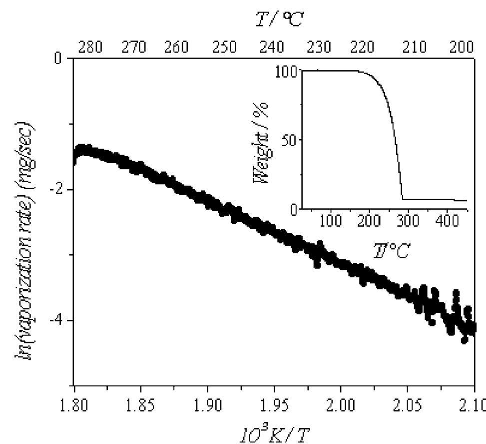

Figure 1. Atmospheric pressure TG vaporization rate of $Bi(C_6H_5)_3$ as function of temperature. The inset shows the TG curve.

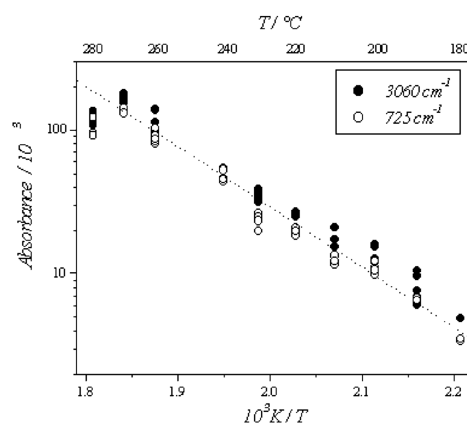

Figure 2. Relevant IR absorbances vs sublimation temperature: (●) 3060 cm^{-1} (νCH); (○) 725 cm^{-1} (γCH).

The TG vaporization rate and the TG curve of $Bi(C_6H_5)_3$ at atmospheric pressure are shown in Figure 1. There is evidence of a clean single-step sublimation occurring in the 160−280 °C temperature range.

FT-IR in situ monitoring was adopted to evaluate the precursor stability during the sublimation and the mass transport to the reaction zone under pure Ar flow (100 sccm).

The aromatic C−H stretching at 3060 cm^{-1} (νCH) and the C−H out-of-plane bending at 725 cm^{-1} (γCH) were used as reference frequencies for $Bi(C_6H_5)_3$.

Gas-phase IR spectra in the 180−280 °C range are similar to solid-state data, thus indicating that sublimation and mass transport do not involve any decomposition. Figure 2 shows the Arrhenius plot of absorbance values of reference frequencies vs $1/T$ in the 180−280 °C range. There is evidence of linear behavior in the entire interval as expected for clean sublimation.

FT-IR Monitoring of MOCVD Processes. $Bi(C_6H_5)_3$ decomposition was studied by in situ FT-IR monitoring of the gas phase during the MOCVD process.

Figure 3 shows gas-phase spectra (4000−600 cm^{-1}) of $Bi(C_6H_5)_3$ for several temperatures in the 200−500 °C range under Ar/O_2 (1:5) flow. An enlargement of the spectral region between 775 and 625 cm^{-1} is shown in Figure 4. No relevant spectral changes are observed between 200 and 350 °C. At 400 °C, the γCH band, which is typical only for monosubstituted aromatic rings, decreases, whereas a new peak appears at 671

(48) Temple, D.; Reisman, A. *J. Electrochem. Soc.* **1989**, *11*, 136.
(49) Colthup, N. B.; Daly, L. H.; Wibiberley, S. E. *Introduction to Infrared and Raman Spectroscopy*; Academic Press: New York, 1964; p 220.
(50) Nakamoto, K. *Infrared and Raman Spectra of Inorganic and Coordination Compounds*; John Wiley and Sons: New York, 1978.

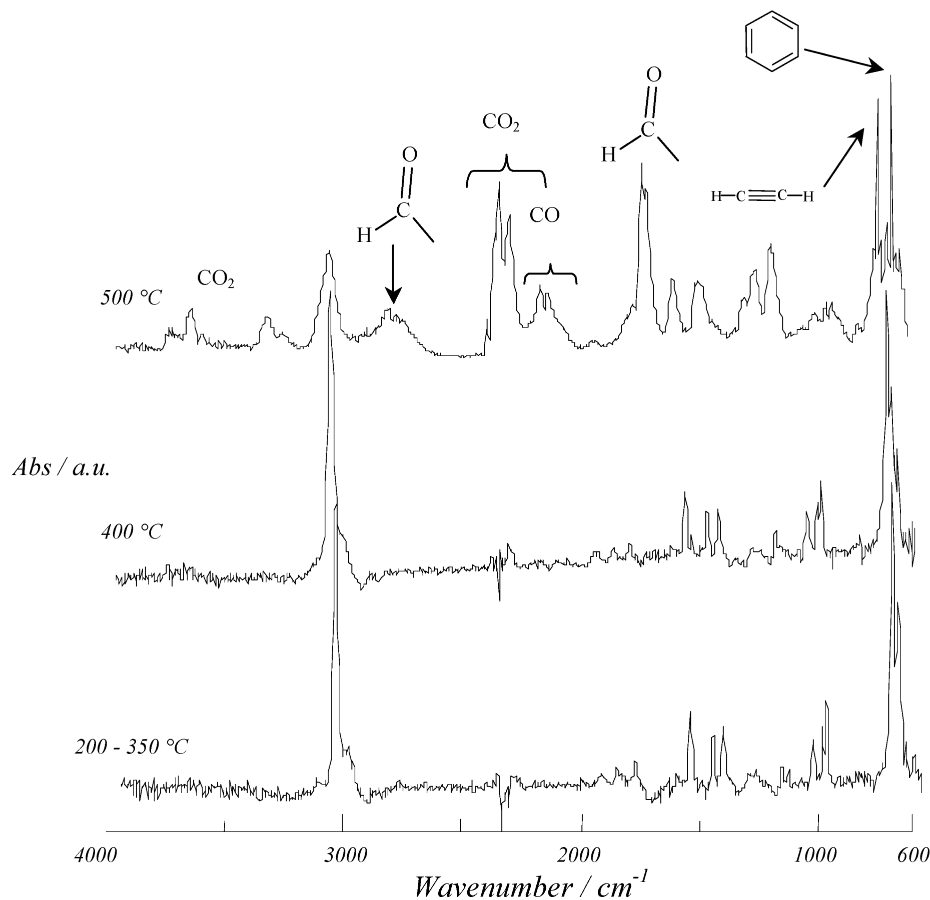

Figure 3. In situ IR spectra of $Bi(C_6H_5)_3$ at various deposition temperatures under Ar/O_2.

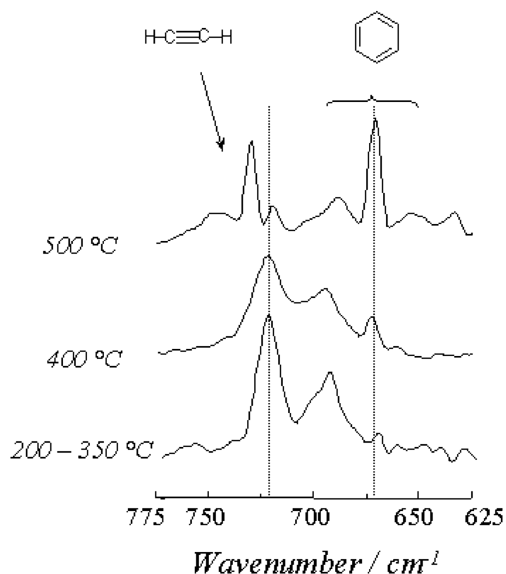

Figure 4. IR spectral region from 625 to 775 cm^{-1} of $Bi(C_6H_5)_3$ at various deposition temperatures under Ar/O_2.

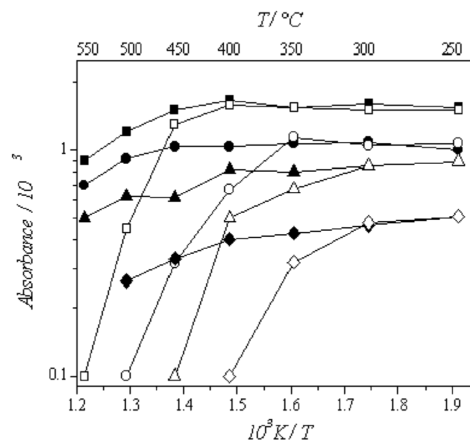

Figure 5. Dependence of the absorbance of bands at 3060 cm^{-1} (νCH) and at 725 cm^{-1} (γCH) of $Bi(C_6H_5)_3$ vs deposition temperature under Ar/O_2 at various P_{Bi}: (■) νCH; (□) γCH at P_{Bi} = 19 mTorr; (●) νCH; (○) γCH at P_{Bi} = 16 mTorr; (▲) νCH; (△) γCH at P_{Bi} = 13 mTorr; (◆) νCH; (◇) γCH at P_{Bi} = 5 mTorr.

cm^{-1} that can be associated with the C−H out-of-plane bending of benzene in gas phase.[49] The other band of C_6H_6 at 3070 cm^{-1} is hidden by the IR band of the undecomposed precursor at 3060 cm^{-1}. Note that the formation of C_6H_6 was also observed in the decomposition of $Bi(C_6H_5)_3$ powders.[26] At 500 °C the band at 725 cm^{-1} disappears and new IR modes associated with different byproducts become evident.

The new IR modes consist of (i) typical doublets centered at 2295 and 2163 cm^{-1} associated with CO_2 and CO molecules; (ii) bands at 1730 and 2800 cm^{-1} due to C=O stretching and C−H stretching of aldehydes; (iii) bands at 3310 and 730 cm^{-1} due, respectively, to C−H stretching and bending of acetylene. These features can be associated with both the oxidative breaking of the aromatic ring as well as oxidation byproducts.

Figure 5 shows the temperature dependence of the absorbance due to νCH and γCH for four different partial pressures of $Bi(C_6H_5)_3$ (5, 13, 16, and 19 mTorr). Different behavior of these two IR modes is evident in all cases. The absorption due to νCH of the aromatic ring remains almost unchanged up to 450 °C, while the

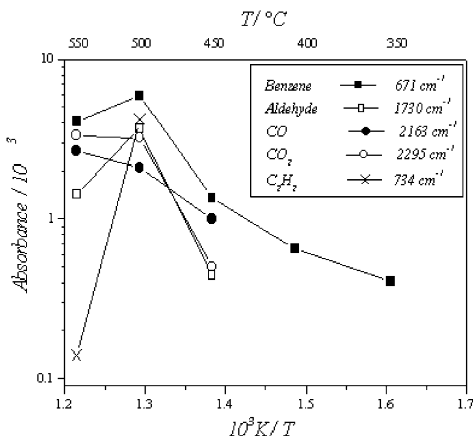

Figure 6. Dependence of the absorbance of main decomposition products vs deposition temperature under Ar/O_2 (P_{Bi} = 13 mTorr) ((●) 2163 cm^{-1} (C−O stretches) of CO; (○) 2295 cm^{-1} (C−O stretches) of CO_2; (□) 1730 cm^{-1} (C═O stretches) of aldehyde; (■) 671 cm^{-1} (C−H out-of-plane bending of benzene).

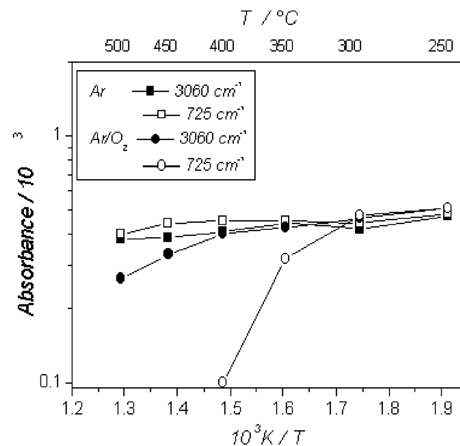

Figure 7. Temperature dependence of bands at 3060 cm^{-1} (νCH) and at 725 cm^{-1} (γCH) of $Bi(C_6H_5)_3$: (●) νCH; (○) γCH adopting Ar/O_2 flow and (■) νCH; (□) γCH adopting Ar flow.

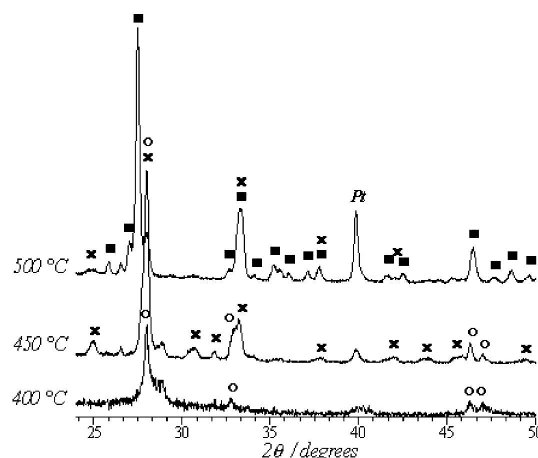

Figure 8. Typical XRD patterns of samples obtained on Pt at various deposition temperatures: (○) tetragonal β-Bi_2O_3 phase, (×) cubic Bi_2O_3 phase, and (■) monoclinic α-Bi_2O_3 phase.

γCH absorption suffers from a sharp decrease in the 350−450 °C range. These results indicate that below 450 °C the decomposition pathway likely involves breakdown of the Bi−phenyl bond leaving the aromatic ring intact.

By contrast, above 450 °C, the band at 3060 cm^{-1} slightly decreases, thus suggesting that a further decomposition involving the breakdown of the aromatic ring is operating.

The P_{Bi} plays a significant role in the $Bi(C_6H_5)_3$ decomposition process. In particular, at P_{Bi} lower than 16 mTorr, the decrease of the γCH band intensity is already detectable at 350 °C, while at higher P_{Bi} values decomposition is significant at higher temperatures. Therefore, the efficiency of the break-down of the Bi−phenyl bond decreases with P_{Bi} increase. This behavior is consistent with a heterogeneous reaction on the reactor walls whose active sites become saturated at high P_{Bi}.

By contrast, the decomposition of the aromatic ring, monitored by the decrease of νCH absorption, is more relevant at higher P_{Bi}.

Figure 6 shows the temperature dependence of the absorbance of the bands due to the main decomposition products at P_{Bi} = 13 mTorr. Free C_6H_6 becomes detectable at 350 °C and its concentration increases at higher temperatures. This observation further supports that decomposition process involves the phenyl dissociation. Above 400 °C, the concentration of CO_2 and CO increases with the temperature, as expected. The concentration of other products of ring breakdown (such as C_2H_2 and aldehydes) shows a maximum at 500 °C.

In Figure 7 the FT-IR data of experiments under pure Ar are compared with those under the Ar/O_2 mixture (1:5) (P_{Bi} = 5 mTorr). As shown in the previous paragraphs, under the Ar/O_2 mixture precursor decomposition is observable at 350 °C. By contrast, under Ar the intensity of the FT-IR bands does not change markedly with temperature. This is evidence that no relevant decomposition processes occur in the absence of oxygen. These results indicate that O_2 plays a crucial role in the film growth through a modulation of the decomposition process.

MOCVD of Bismuth Oxides. Bismuth oxides were deposited on Pt and Ir substrates using the $Bi(C_6H_5)_3$ source under Ar/O_2 flow in the 350−550 °C temperature range (P_{Bi} = 2 mTorr). GIXRD patterns of films deposited over Pt at 400, 450, and 500 °C are shown in Figure 8. At 400 °C, the intense reflection at 28.0° suggests the presence of either cubic or tetragonal phases. However, the Bragg reflections at 33.4°, 46.6°, and 47.4° point to the tetragonal Bi_2O_3 phase, in agreement with earlier MOCVD results.[51] At 450 °C, Bi_2O_3 crystallites are mainly in cubic symmetry, even though the tetragonal phase is still present. Trace of nonstoichiometric oxides (such as $Bi_2O_{2.33}$) are also present. At 500 °C, films consist mainly of the monoclinic α−Bi_2O_3 phase with a few traces of the cubic phase.

Figure 9 shows GIXRD patterns of film growth at various temperatures on Ir substrates. Slight differences can be observed relative to the Pt substrate. At 400 °C, the broader reflections of Bi_2O_3 phase suggest smaller crystallites than those observed on Pt. The poor crystallization does not allow unambiguous determination of the Bi_2O_3 phase obtained, even though the broad envelope around 47° is consistent with the patterns of tetragonal β-Bi_2O_3 phase. At 450 °C, Bi_2O_3 crystallizes mainly in a cubic symmetry. However on the Ir substrate, monoclinic α−Bi_2O_3 oxides are also present in

(51) Barreca, D.; Rizzi, G. A.; Tondello, E. *Thin Solid Films* **1998**, *333*, 35.

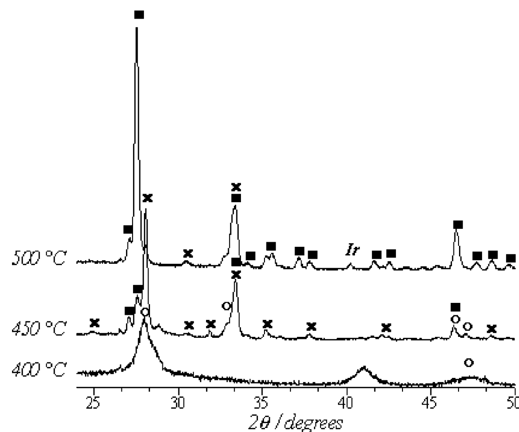

Figure 9. Typical XRD patterns of samples obtained on Ir at various deposition temperatures: (○) tetragonal β-Bi_2O_3 phase, (×) cubic Bi_2O_3 phase, and (■) monoclinic α-Bi_2O_3 phase.

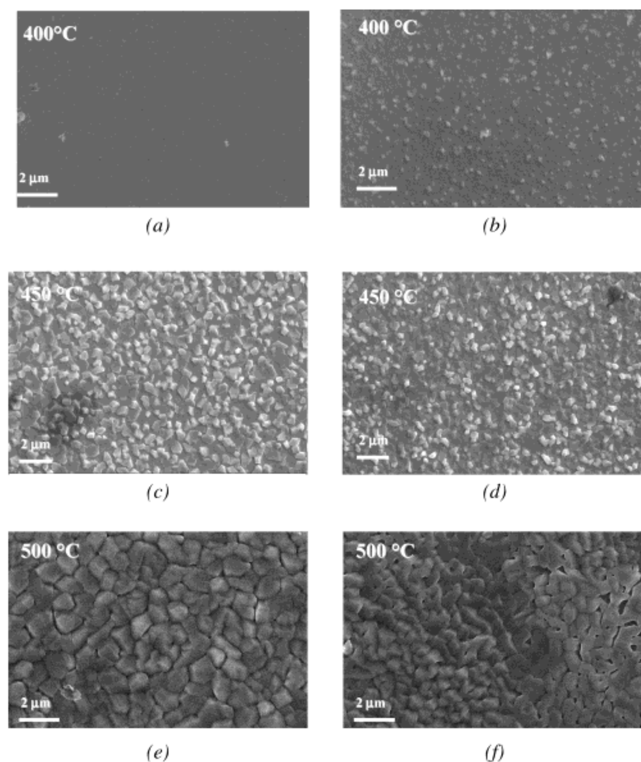

Figure 10. SEM micrographs of films deposited on Ir (a, c, and e) and on Pt (b, d, and f) at various deposition temperatures.

small quantities. At 500 °C, no differences are apparent relative to the Pt substrate.

The average crystallite size was determined using GIXRD data and the Scherrer and Warren equation.[52] The resulting data indicate that crystallite size slightly increases with temperature. On Pt, it ranges from 25 nm at 400 °C to 35 and 40 nm at 450 and 500 °C, respectively. On Ir the crystallite size of film deposited at 400 °C is lower, (10 nm) compared to film deposited on Pt at the same temperature. At temperatures ≥450 °C, crystallite sizes on Ir and Pt are similar.

Morphologies of films deposited on Pt and Ir at various temperatures were inspected by SEM. The observed grains are bigger than crystallites and they

(52) Warren, B. E. *X-ray Diffraction*; Addison-Wesley: Reading, MA, 1969.

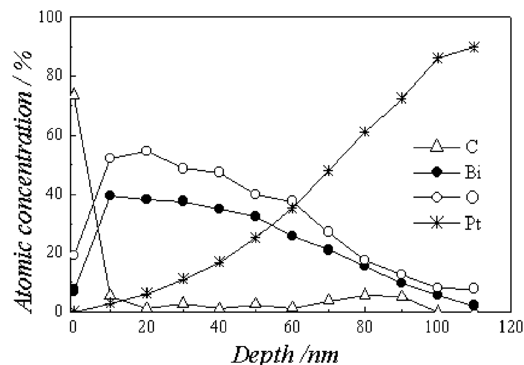

Figure 11. Typical XPS depth profile of a Bi_2O_3 film deposited at 400 °C.

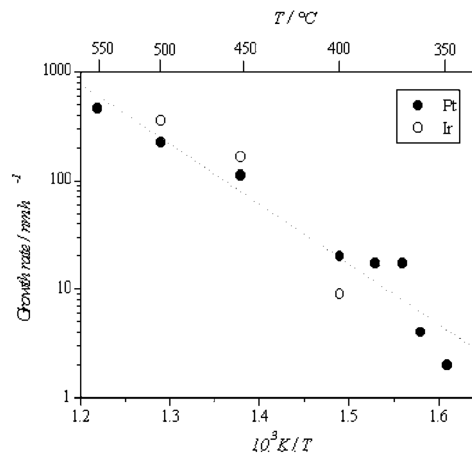

Figure 12. Dependence of the deposition rate vs deposition temperature on (●) Pt and (○) Ir (P_{Bi} = 2 mTorr).

can be considered crystallite agglomerates. There is evidence that morphology depends on temperature and substrate nature, analogously to GIXRD results. Larger crystallite agglomerates are formed upon increasing deposition temperature. In particular, at 400 °C particles are scarcely visible in the films grown on Ir, while bigger grains can be observed on Pt (Figure 10a and b). As expected, at 450 and 500 °C (Figure 10c, d, e, and f), the size of the crystallite agglomeration increases, respectively, from 500 nm to 1 μm for both substrates, even though the size on Ir is larger than that on Pt.

The purity of Bi_2O_3 films deposited under Ar/O_2 was studied by XPS depth profiles. No carbon contamination was observed in the films deposited in the 350−500 °C range. Figure 11 shows a typical profile of a film deposited at 400 °C. Note that the observed O/Bi ratio is slightly lower than the value expected for pure Bi_2O_3. This result can suggest the presence of oxygen vacancies in the film even though possible sputter-related reduction cannot be ruled out.

Kinetics of the Deposition Process. Further insights into deposition processes were obtained by evaluating the dependence of the Bi_2O_3 growth rate upon various parameters namely (i) the substrate, (ii) the deposition temperature, and (iii) P_{Bi}.

Figure 12 shows the variation of the deposition rate of Bi_2O_3 on Pt and Ir substrates as a function of the temperature above 350 °C (P_{Bi} = 2 mTorr). Note that this temperature represents the onset of film deposition on Pt.[46] The plot of growth rate log vs $1/T$ for both substrates is linear. This indicates that the Bi_2O_3

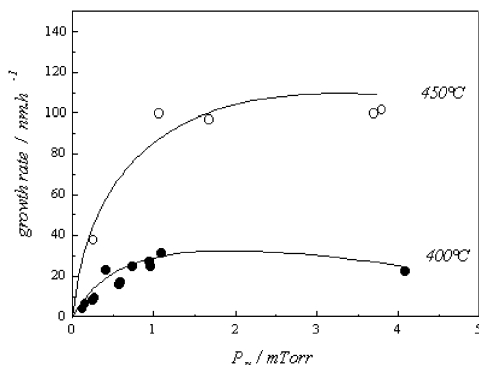

Figure 13. Dependence of the growth rate on P_{Bi} adopting Pt substrates at two different deposition temperatures: (●) 400 °C; (○) 450 °C. Solid lines represent theoretical curves calculated according to the Langmuir–Hinshelwood model.

deposition occurs under the reaction rate-limited regime in the overall temperature range. The apparent activation energy (E_{Bi}) on both Pt and Ir is 100 ± 10 kJ/mol.

Figure 13 shows the dependence of growth rate upon P_{Bi} in the 0.1–4.2 mTorr range at 400 and 450 °C. The deposition rate increases with the precursor partial pressure until maximum values (30 and 100 nm/h at 400 and 450 °C, respectively) are reached at $P_{Bi} > 1$ mTorr. These values are nearly constant (within ± 10 nm/h) in the investigated P_{Bi} range, even though a slight decay can be observed above 4 mTorr (at $T = 400$ °C). This behavior indicates that the rate-limiting step involves a surface reaction where the active sites of the substrate become saturated under $Bi(C_6H_5)_3$ partial pressure higher than 1 mTorr.

MOCVD Mechanisms. On the basis of FT-IR and kinetic data it is possible to model the MOCVD process. There is evidence that the $Bi(C_6H_5)_3$ precursor is transported intact to the deposition zone where it decomposes above 300 °C.

In the 350–450 °C range, in situ FT-IR results point to a decomposition process involving the breakdown of the Bi–phenyl bond and the formation of free benzene. Moreover, the FT-IR investigation has shown evidence that O_2 plays a relevant role in the MOCVD process since it promotes $Bi(C_6H_5)_3$ dissociation, thus favoring the Bi_2O_3 growth.

Both FT-IR data and growth rate dependence upon P_{Bi} reported in Figure 13 are consistent with a heterogeneous mechanism based on the Lagmuir–Hinshelwood model.[53] This model has been often applied to describe the MOCVD of several metals and oxides in the presence of H_2 or O_2.[54–57] According to this model, deposition proceeds through the adsorption of $Bi(C_6H_5)_3$ and O_2 on adjacent surface sites, followed by their interaction, leading to the dissociation of some of the phenyl groups as benzene and to Bi_2O_3 formation. Hydrogen required for benzene release could be provided by –OH groups on the surface of the SiO_2 reactor walls or of the Bi_2O_3 film if traces of water are present. Moreover, it is also possible that the breakdown of Bi–phenyl bonds is followed by the combustion of a small fraction of the aromatic rings. This last process leads to hydrogen containing byproducts (such as water), which give the H atoms needed for the formation of benzene.

According to a simple Langmuir–Hishelwood model, the fractions of the surface occupied by $Bi(C_6H_5)_3$ and O_2 (θ_{Bi} and θ_{O_2} respectively) are

$$\theta_{Bi} = \frac{K_{Bi} \times P_{Bi}}{(1 + K_{Bi}P_{Bi} + K_{O_2}P_{O_2})} \quad (1)$$

$$\theta_{O_2} = \frac{K_{O_2} \times P_{O_2}}{(1 + K_{Bi}P_{Bi} + K_{O_2}P_{O_2})} \quad (2)$$

where P_{O_2} is the oxygen partial pressure and K_{Bi} and K_{O_2} are the equilibrium constants for precursor and oxygen adsorptions.

Neglecting possible dissociation process of adsorbed species, the reaction rate is assumed proportional to $\theta_{Bi} \times \theta_{O_2}$.

$$\text{Rate} = \frac{k \times K_{O_2}K_{Bi} \times P_{Bi}P_{O_2}}{(1 + K_{Bi}P_{Bi} + K_{O_2}P_{O_2})^2} \quad (3)$$

where k is a reaction constant.

Keeping P_{O_2} constant, eq 3 can be rewritten as

$$\text{Rate} = \frac{k' \times P_{Bi}}{(1 + k''P_{Bi})^2} \quad (4)$$

with

$$k' = \frac{kK_{O_2}K_{Bi}P_{O_2}}{(1 + K_{O_2}P_{O_2})^2} \text{ and } k'' = \frac{K_{Bi}}{(1 + K_{O_2}P_{O_2})}$$

The rate equation (eq 4) shows that growth rate increases with P_{Bi} until a maximum value and decays for higher values. This trend is not only consistent with the found data of the growth rate (Figure 13), but also with the results regarding the decreased efficiency of the Bi–phenyl dissociation observed in the FT-IR experiments by increasing P_{Bi}.

The proposed heterogeneous mechanism is not surprising since the catalytic activity under O_2 of the various Bi_2O_3 polymorphs is well-known.[3,58,59] In fact, studies on the interaction of molecular oxygen with bismuth oxides showed that β-Bi_2O_3 was capable of activating adsorbed O_2 through the formation of chemisorbed O_2^- on oxygen vacancies.[3]

Above 450 °C, FT-IR spectra show the presence of oxidation byproducts (CO_2, CO, C_2H_2, aldehydes) likely due to ring opening/breaking, thus suggesting the onset of more complex decomposition processes. Note that similar products have already been reported in several studies on benzene (and substituted benzene) decom-

(53) Bond, G. C. *Catalysis by Metals*; Academic Press: London and New York, 1962; p 123.
(54) Borgharkar, N. S.; Griffin, G. L. *J. Electrochem. Soc.* **1998**, *145*, 347.
(55) Brissonneau, L.; Reynes, A.; Vahlas, C. *Chem. Vap. Deposition* **1999**, *5*, 281.
(56) Cheng, W. Y.; Hong, L. S. *Thin Solid Films* **2002**, *415*, 94.
(57) Condorelli, G. G.; Malandrino, G.; Fragalà, I. L. *Chem. Vap. Deposition* **1999**, *5*, 21.
(58) Mehandru, S. P.; Anderson, A. B.; Brazdil, J. F. *J. Chem. Soc., Faraday Trans. 1* **1987**, *83*, 463.
(59) Driscoll, D. J.; Martir, W.; Lunsford, J. H. *J. Phys. Chem.* **1987**, *91*, 3585.

Chart 1. Schematic Picture Showing the Two Main Decomposition Pathways of $Bi(C_6H_5)_3$ during MOCVD Processes

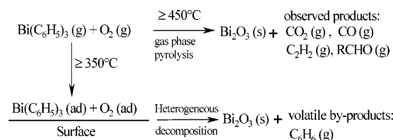

position in the presence of oxygen.[60−62] In particular, it is known that both heterogeneous and homogeneous decomposition processes lead mainly to CO_2 and CO. In addition, theoretical and experimental works on homogeneous combustion of benzene (and phenyl-substituted compounds) report acetylene and species containing −CHO groups among the main products.[62] Therefore, a similar homogeneous decomposition can be proposed for $Bi(C_6H_5)_3$ above 450 °C. FT-IR data are consistent with this hypothesis since they show that ring breakdown at high temperature is more evident for high P_{Bi} indicating a different nature compared to the low-temperature heterogeneous process.

A schematic picture of the two main pathways is displayed in Chart 1.

Conclusions

Insights about the Bi_2O_3 MOCVD process adopting the $Bi(C_6H_5)_3$ precursor have been obtained. $Bi(C_6H_5)_3$ possesses suitable thermal stability upon sublimation and good mass-transport properties and so proves to be an appropriate source for Bi-based materials. However, experiments have shown that O_2 plays a determining role in efficient precursor decomposition, thus suggesting that $Bi(C_6H_5)_3$ is well suited for deposition processes under oxidizing atmosphere, but less appropriate when oxygen has to be avoided. The gas-phase in situ FT-IR data and the growth kinetics support the following model for the MOCVD process: in the 350−450 °C temperature range the deposition mechanism involves a heterogeneous pathway leading to the dissociation of Bi−phenyl bonds and the formation of polycrystalline Bi_2O_3. Above 450 °C, other decomposition pathways, involving the oxidative breakdown of the aromatic ring, also occur. These lead to various oxidation products and, therefore, to less clean processes.

Deposition temperatures (≥350 °C) higher than other Bi sources are required to obtain significant growth rates. This clearly depends on the greater thermal stability of $Bi(C_6H_5)_3$. The present data are of relevance not only for the optimization of MOCVD deposition of Bi_2O_3 but, even more important, for the fabrication of multicomponent materials such as SBT and BLT. For these applications, a more complete knowledge of the precursor chemistry during the MOCVD process is a key point both for the choice of the best-suited precursor combination and for the design of new precursors with optimized decomposition routes.

Acknowledgment. We gratefully thank the European Commission (IST-2000-30153-FLEUR contract) and MIUR (FIRS project) for financial support.

CM049836H

(60) Wu, W. C.; Liao, L. F.; Lien, C. F.; Lin, J. L. *Phys. Chem. Chem. Phys.* **2001**, *3*, 4456.
(61) Viste, M. E.; Gibson, K. D.; Sibener, S. J. *J. Catal.* **2000**, *191*, 237.
(62) Fadden, M. J.; Hadad, C. M. *J. Phys. Chem. A* **2000**, *104*, 8121.